



# Nickel porphyrin/ZnIn<sub>2</sub>S<sub>4</sub> heterojunction with Ni-S highway for boosting charge separation and visible-light-driven H<sub>2</sub> production

Huaiyang Jia, Xinxin Shao, Ya'nan Wang, Jing Zhang, Renjie Li <sup>\*</sup>, Tianyou Peng <sup>\*</sup>

College of Chemistry and Molecular Sciences, Engineering Research Center of Organosilicon Compounds & Materials, Wuhan University, Wuhan 430072, China



## ARTICLE INFO

**Keywords:**  
Hydrogen evolution reaction  
Nickel porphyrin  
ZnIn<sub>2</sub>S<sub>4</sub>  
Type II heterojunction  
Ni-S channel

## ABSTRACT

Due to the exceptional potential to retard the charge recombination, semiconductor-based heterojunctions as photocatalysts have attracted extensive attention. Herein, nickel(II) 5,10,15,20-tetraphenyl-21H,23H-porphyrin (NiTPP) and ZnIn<sub>2</sub>S<sub>4</sub> (ZIS) fluorinated microspheres are used to construct a novel inorganic-organic heterojunction (NiTPP/ZIS). Compared with the NiTPP and ZIS, the resultant NiTPP/ZIS exhibits enhanced optical absorption, charge separation and photoelectrochemical behavior. Further investigations demonstrate that a type II heterojunction mechanism proceeds in the NiTPP/ZIS heterojunction to boost the charge separation *via* the Ni-S highway formed between the NiTPP and ZIS components. No need of additional cocatalyst, the NiTPP/ZIS heterojunction with an optimal mass ratio delivers a superior apparent quantum yield of 64.0% at 400 nm and a remarkable H<sub>2</sub> evolution activity of 2305  $\mu\text{mol h}^{-1}$  under visible light ( $\lambda \geq 400$  nm) irradiation, 10 and 256 times higher than that of the ZIS and NiTPP alone, respectively. This work presents a new concept for constructing inorganic-organic heterojunctions for high-performance artificial photosynthesis systems.

## 1. Introduction

The need for eco-friendly and sustainable energy revolution is growing more and more urgent due to the massive emissions of greenhouse gases and the increasing depletion of fossil fuels. Hydrogen (H<sub>2</sub>) is supposed to be the most viable option because of its high energy density and green energy cycle [1–3]. Photocatalytic H<sub>2</sub> evolution reaction driven by solar energy, in particular, has drawn a lot of attention lately due to its high utility, non-toxicity and renewable nature [4]. Hence, a vast array of semiconducting materials including TiO<sub>2</sub>, C<sub>3</sub>N<sub>4</sub> and CdS have been developed as photocatalysts [5–7]. However, the majority of inorganic photocatalysts exhibit relatively narrow spectral responsive range, fast charge recombination, low durability and poor solar energy conversion efficiency, making the photocatalytic H<sub>2</sub> production technology insufficient to large-scale application [8–10]. In this sense, further exploration of the key influencing factors of H<sub>2</sub> evolution reaction lies in the development of novel photocatalysts with superior activity and excellent stability [11]. On the other hand, many reports have figured out that the photocatalytic performance of a single photocatalyst is generally constrained by the unsuitable band edge positions and the rapid charge recombination [12]. Therefore, a number of techniques, such as cocatalyst loading [10], element doping [13], defect engineering

[14,15], interfacial modulating [16] and heterojunction (e.g. type II, Z-scheme or p-n junction) constructing [17,18], have been developed to improve the photoactivity. Among them, constructing heterojunctions is of particular interest in the point of enlarging light harvesting, accelerating charge separation and strengthening stability [19,20].

In natural photosynthesis, chlorophylls plays a key role, and thus its analogs, metalloporphyrin derivatives, have been studied as photosensitizer and/or photocatalyst to promote the energy conversion efficiency [17,21]. Besides, metalloporphyrins not only possess suitable conjugated structure, but also have multiplicity of substituents and abundant flexibility of central metal ions, making them ideal for combining with inorganic semiconductors to bridge tight charge transfer channel [21, 22]. Recent researches on asymmetric zinc porphyrins have revealed that the types of substituents and steric positions of the same substituent group can influence the electron transfer of the catalytic units [23]. Besides, the central metals of metalloporphyrins were studied as the main factor causing distinct photosensitization over carbon nitride for visible-light-responsive H<sub>2</sub> production [24]. What's more, a direct Z-scheme mechanism in a novel hybrid material *via* H-bonding formed between chromium-5-(4-carboxyphenyl)-10,15,20-triphenylporphyrin and BiVO<sub>4</sub> nanosheets achieved boosted overall water splitting with an apparent quantum yield up to 8.47 % at 400 nm [17]. The above

\* Corresponding authors.

E-mail addresses: [lirj@whu.edu.cn](mailto:lirj@whu.edu.cn) (R. Li), [typeng@whu.edu.cn](mailto:typeng@whu.edu.cn) (T. Peng).

results demonstrate the great application potential of metalloporphyrins in the field of photocatalysis.

$\text{ZnIn}_2\text{S}_4$ , as a member of ternary chalcogenide family, has an admirable bandgap (2.06–2.85 eV) and strong capacity to harvest visible light, coming into the spotlight as an intriguing photocatalyst for  $\text{H}_2$  evolution [12,18,25–30]. Therefore, combining  $\text{ZnIn}_2\text{S}_4$  and metal porphyrin derivative to construct inorganic-organic heterojunctions for  $\text{H}_2$  production is a feasible route. Herein, with nickel(II) 5,10,15, 20-tetraphenyl-21H,23H-porphyrin (NiTPP) and  $\text{ZnIn}_2\text{S}_4$  (ZIS) floriated microspheres as raw materials, a novel organic-inorganic heterojunction (NiTPP/ $\text{ZnIn}_2\text{S}_4$ ) is constructed through a facile reflux process. The optical absorption, photoinduced charge separation, photoelectrochemical behavior and photocatalytic performance of the resultant NiTPP/ZIS heterojunction are studied in detail. A type II heterojunction mechanism with boosted charge separation via the Ni-S highway formed between the NiTPP and ZIS components is demonstrated. No need of additional cocatalyst, the resultant NiTPP/ZIS heterojunction with an optimal mass ratio achieves a superior apparent quantum yield of 64.0 % at 400 nm and a remarkable  $\text{H}_2$  evolution activity of 2305  $\mu\text{mol h}^{-1}$  under visible light ( $\lambda \geq 400$  nm) irradiation, 10 and 256 times higher than that of ZIS and NiTPP alone, respectively. This study not only provides an efficient strategy for constructing heterojunction with Ni-S channel to boost the charge carrier mobility and the  $\text{H}_2$  evolution activity, but also presents a novel concept for constructing inorganic-organic hybrid materials for high-performance artificial photosynthesis systems.

## 2. Experimental section

### 2.1. Material preparation

Nickel(II) 5,10,15,20-tetraphenyl-21H,23H-porphyrin (NiTPP) was synthesized using 5,10,15,20-tetraphenyl-21H,23H-porphyrin ( $\text{H}_2\text{TPP}$ ) according to our previous report [31]. In brief, 98.4 mg (0.16 mmol) of  $\text{H}_2\text{TPP}$  and 159.3 mg (0.64 mmol) of  $\text{Ni}(\text{CH}_3\text{COO})_2 \cdot 4\text{H}_2\text{O}$  were added in a flask, and then sealed, degassed and pumped with high-purity  $\text{N}_2$  gas, followed by injecting 40 mL of N,N-dimethylformamide (DMF). The mixture was refluxed at 150 °C for 12 h under stirring. After that, the suspension was washed with deionized water six times, and then purified via column chromatogram with dichloromethane/n-hexene (1:2, v/v) as eluting solvent. The product was recrystallized in the dichloromethane/n-hexane solvent, and then dried overnight at 65 °C in vacuum oven to obtain the NiTPP (Yield: 91 mg, 85 %. TOF-MS( $m/z$ ) calcd. for  $\text{C}_{44}\text{H}_{28}\text{N}_4\text{Ni} [\text{M}+\text{H}]^+$ : 671.4, found 671.1 (Fig. S1)).

$\text{ZnIn}_2\text{S}_4$  (ZIS) floriated microspheres were prepared through a precipitation method [26]. Typically, 136.3 mg (1.0 mmol) of  $\text{ZnCl}_2$ , 442.3 mg (2.0 mmol) of  $\text{InCl}_3$ , 300.5 mg (4.0 mmol) of thioacetamide and 8.0 mL of ethylene glycol were added into 32 mL of deionized water, which pH value was adjusted to 2.50 using HCl solution (1.0 M). Under stirring, the mixed solution was heated at 80 °C for 3 h with an oil bath. The precipitate was washed with deionized water and ethanol three times in sequence, and then dried at 65 °C in vacuum oven to obtain the ZIS floriated microspheres.

NiTPP/ZIS heterojunction was prepared through a reflux method. Typically, 7.5 mg of NiTPP was dissolved in 40 mL of DMF, and then 42.5 mg of ZIS was added into the solution. The mixture was put in ultrasonic bath for 1 h and heated at 120 °C for 6 h with intermittent stirring. After cooling down, the solvent was distilled by rotary evaporation under vacuum, and the solid was washed with deionized water three times, and then dried at 65 °C in vacuum oven to obtain the 15 wt % NiTPP/ZIS. By varying the addition amount of NiTPP, a series of NiTPP/ZIS heterojunctions with various mass ratios were prepared. Besides, 15 wt%  $\text{H}_2\text{TPP}/\text{ZIS}$  was also synthesized by using  $\text{H}_2\text{TPP}$  and ZIS for comparison.

Pt-loaded NiTPP/ZIS heterojunction (Pt-(NiTPP/ZIS)) was prepared through a photodeposition procedure. Typically, 0.20 g of NiTPP/ZIS

was dispersed in 120 mL of deionized water containing methanol (45 mL) and  $\text{H}_2\text{PtCl}_6$  solution (133  $\mu\text{L}$ , 0.077 M) in a Pyrex cell. After sealed with cling film and irradiated with a 500 W Hg-lamp for 3 h, the product was washed with deionized water and ethanol three times in sequence, and then dried overnight in vacuum at 80 °C to obtain the 1.0 wt% Pt-(NiTPP/ZIS). Likewise, Pt-NiTPP/ZIS and NiTPP/Pt-ZIS were also prepared via the same procedure of the NiTPP/ZIS using 1.0 wt% Pt-NiTPP or 1.0 wt% Pt-ZIS.

### 2.2. Material characterization

Crystal phase studies of the samples were based on the X-ray diffraction (XRD) patterns acquired on a Miniflex 600 X-ray diffractometer with a  $\text{CuK}\alpha$  irradiation operating at 40 kV, 15 mA and a scan rate of 10°  $\text{min}^{-1}$ . Elemental analyses (CHN) were performed on a German elemental analyzer (Vario EL cube) after the material was dried, pulverized uniformly and then wrapped in a tin boat and evaluated using the general rule of element analyzer method (JY/T017–1996). The Ni contents in NiTPP and its hybrid materials were measured using an IRIS Intrepid II XSP inductively coupled plasma-atomic emission spectrometer (ICP-AES). The Zn/In/S element contents were determined using a JXA-8530F Plus Field Emission Electron Probe Analyzer (EPMA).

A BIORAD FTS-165 Fourier transform infrared (FTIR) spectrometer was utilized to identify the FTIR spectra in the region of 4000–400  $\text{cm}^{-1}$  using KBr disk. A Thermo Scientific iS50 Raman microscope with  $\lambda_{\text{ex}} = 1064$  nm was used to measure the Raman spectra. With a standard and monochromatic source ( $\text{AlK}\alpha$ ), a Thermo-Fisher ESCALAB 250Xi X-ray photoelectron spectroscope (XPS) operating at 300 W was employed to acquire the XPS spectra, which were calibrated with the C 1s derived from polytetrafluoroethylene. A Shimadzu UV-3600 UV–VIS–NIR spectrophotometer was used to acquire the UV–vis diffuse reflectance absorption spectra (DRS) with  $\text{BaSO}_4$  as reference. A Hitachi F-6000 fluorescence spectrophotometer was adopted to detect the photoluminescence (PL) spectra. With an excitation wavelength of 375 nm and an emission wavelength of 469 nm, an Edinburgh FES 920 femtosecond fluorescence spectrophotometer was utilized to get the time-resolved photoluminescence (TRPL) spectra. The morphologies and microstructures of the samples were observed on a Zeiss Merlin compact field emission scanning electron microscope (FESEM) using an accelerating voltage of 5.0 kV and a JEOL LaB6 JEM-2100(HR) high-resolution transmission electron microscope (HRTEM) operating at 200 kV. A JEOL SDD-detector with two 100  $\text{mm}^2$  X-ray sensors was used to perform the energy-dispersive X-ray spectroscopy (EDX) elemental mappings.

A CHI750E electrochemical workstation with a three-electrode system was employed for the (photo)electrochemical measurements with  $\text{Na}_2\text{SO}_4$  solution (0.5 M) as electrolyte. Pt foil and  $\text{Ag}/\text{AgCl}$  (with KCl saturated aqueous solution) were chosen to be the counter electrode and the reference electrode, respectively. Working electrode was made as follows: 3.0 mL of Nafion ethanol solution (0.05 wt%) contained 10.0 mg of catalyst was treated with an ultrasonic bath for 3 h. The suspension was stirred overnight before being applied to the pre-cleaned fluorine-doped tin oxide (FTO) glass, which was then dried naturally at room temperature to give the working electrode. The potentials were transferred into normal hydrogen electrode (NHE) utilizing the equation of  $E_{\text{NHE}} = E_{\text{Ag}/\text{AgCl}} + 0.1981$  V.

Electrochemical impedance spectrum (EIS) was observed at a potential of 0 V vs. NHE with a frequency range of 0.05 Hz up to 100 kHz. Time-dependent photocurrent measurements were carried out at a bias potential of 0.30 V vs. NHE and under visible light ( $\lambda \geq 400$  nm) irradiation. The flat band potential ( $E_{\text{fb}}$ ) was measured at the initial potential of  $-0.40$  V vs. NHE and the final potential of 0.20 V vs. NHE, and the  $E_{\text{fb}}$  value was estimated using the Mott-Schottky relation Eq. (1) [5]:

$$C^{-2} = (2/e\epsilon\epsilon_0 N_{\text{d}})[V_{\text{a}} - E_{\text{fb}} - kT/e] \quad (1)$$

where  $C$  is the space charge layer capacitance,  $e$  is the electron charge,  $\epsilon$

is the dielectric constant,  $\epsilon_0$  is the permittivity of vacuum,  $N_d$  is the electron donor density, and  $V_a$  is the potential applied.

The photocurrent ( $J$ ) for water splitting is a product of the rate of photon absorption and charge separation and transfer efficiencies, which can be expressed as  $J = J_{abs} \times \eta_{sep} \times \eta_{trans}$ , where  $J_{abs}$  is the current density,  $\eta_{sep}$  is the photogenerated charge separation efficiency, and  $\eta_{trans}$  is the charge transfer efficiency to the electrolyte. Among them,  $\eta_{sep}$  represents the fraction of photogenerated holes that do not recombine with electrons in the bulk.  $\eta_{trans}$  represents the yield of those holes that reached the electrode/electrolyte interface and that are injected into the electrolyte to oxidize water. The  $\eta_{sep}$  and  $\eta_{trans}$  are calculated using Eqs. (2) and (3) [32,33]:

$$\eta_{sep} = \frac{J_{Na_2SO_3}}{J_{abs}} \times 100\% \quad (2)$$

$$\eta_{trans} = \frac{J_{H_2O}}{J_{Na_2SO_3}} \times 100\% \quad (3)$$

where  $J_{Na_2SO_3}$  and  $J_{H_2O}$  represent the individual photocurrent with  $Na_2SO_3$  solution (as hole scavenger) and deionized water (without hole scavenger) under AM1.5 G illumination, respectively.  $J_{abs}$  is the theoretical maximum photocurrent, estimated at  $5.62 \text{ mA cm}^{-2}$  [34].

### 2.3. Photocatalytic experiments

The photocatalytic  $H_2$  production activity was assessed using a Pyrex glass gas-closed top-irradiation vessel. To be precise, 50 mL of aqueous solution containing 15 vol% triethanolamine (TEOA) as a sacrificial reagent was mixed with 80 mg of catalyst. The suspension was mixed in an ultrasonic bath for 3 min, and then vacuumed to remove oxygen completely. After that, the photoreactor under constant stirring was exposed to the visible light irradiation of a PLS-SXE300 Xe-lamp (Beijing Perfectlight Technology Co. Ltd.) with a cutoff filter ( $\lambda \geq 400 \text{ nm}$ ), in the meanwhile, the temperature of photoreactor is maintained at  $30^\circ\text{C}$  through circulating cooling water. A SP6890 gas chromatograph (GC, TCD detector, 5 Å molecular sieve columns, and Ar as carrier gas) was used to measure the produced  $H_2$  amount. The  $H_2$  production activity was calculated based on the retention time and peak area, which were calibrated with high-purity  $H_2$  gas as standard.

Keeping the same photoreaction conditions, the  $H_2$  generation activities under various monochromatic light irradiations, which were obtained using band-pass filters, were measured. The monochromatic light intensities were determined using an Oriel calibrated Si photodiode (SRC-100-TCQZ-N), and the apparent quantum yields (AQY) were calculated according to Eq. (4):

$$\text{AQY} / \% = \frac{2 \times \text{number of evolved } H_2 \text{ molecules}}{\text{number of incident photons}} \times 100\% \quad (4)$$

### 2.4. Radical quantification experiments

The trapping experiments of active species in an air-containing photoreaction system were carried out for exploring the photocatalytic mechanism of NiTPP/ZIS heterojunction [35]. With terephthalic acid (TA) as probe molecule, the hydroxyl radical ( $\bullet\text{OH}$ ) produced in the photoreaction system was precisely measured using a fluorescence method because TA can react with  $\bullet\text{OH}$  to produce 2-hydroxyterephthalic acid with a strong fluorescence peak at  $\sim 431 \text{ nm}$  when exposed to an excitation wavelength ( $\lambda_{ex}$ ) of 315 nm [35]. Usually, a mixture of TA (0.05 mM) and NaOH (2.0 mM) was made, and then the catalyst (10.0 mg) was added to 50 mL of hydroxyl detection solution while immersed in an ultrasonic bath. After that, visible light ( $\lambda \geq 400 \text{ nm}$ ) was exposed to the mixture while stirring continuously for 1 h. Every 10 min, 3 mL of the clarifying solution were extracted and measured using a Hitachi F-4500 fluorescence spectrophotometer. Since nitro-tetrazolium blue chloride (NBT, 0.025 mM) as probe molecule, which

can react with the superoxide radical ( $\bullet\text{O}_2$ ) produced in the photoreaction system, and thus reducing the absorption maximum at  $\sim 259 \text{ nm}$  of the NBT [35], a TU-1810 UV-Vis spectrophotometer was used to quantify the absorbance decrease of the NBT concentration to examine the  $\bullet\text{O}_2$  amount produced in the photoreaction system. The test protocol was identical to the  $\bullet\text{OH}$  test described above with exception of equilibrating in the dark for 30 min prior to the irradiation.

## 3. Results and discussion

### 3.1. Crystal phase and microstructure analyses

The XRD patterns (Fig. 1a) show that the ZIS displays distinct diffraction peaks at  $2\theta = 21.3^\circ, 27.7^\circ, 30.3^\circ$  and  $47.6^\circ$ , corresponding to the diffractions of (006), (102), (104) and (110) facets of hexagonal  $ZnIn_2S_4$  (JCPDS No. 65-2023) [18], respectively. Meanwhile, the NiTPP exhibits three main peaks at  $2\theta = 15.0^\circ, 19.8^\circ$  and  $25.6^\circ$ , ascribable to the diffractions of (112), (103) and (004) facets of the NiTPP [36]. The NiTPP/ZIS heterojunctions exhibit co-existence of those diffraction peaks of ZIS and NiTPP without obvious shift. Moreover, the diffraction peaks of NiTPP appear an increasing trend along with enhancing the mass ratio of NiTPP. These results suggest the successful formation of the NiTPP/ZIS heterojunction, while the refluxing process does not affect the crystal phase of the ZIS and NiTPP components.

The Raman spectra (Fig. 1b) show that the single ZIS has obvious four characteristic Raman bands at  $249.2, 301.6, 343.0$  and  $370.4 \text{ cm}^{-1}$ , which can be severally assigned to the  $LO_1, TO_2, LO_2$  and  $A_{1g}$  modes of  $ZnIn_2S_4$  [37], respectively. The NiTPP exhibits an obvious active Raman mode of N-Ni bond at  $402.5 \text{ cm}^{-1}$ , while the characteristic bands of the in-plane transitional motion and the out of plane deformation mode of phenyl groups within the porphyrin are located at  $205.0$  and  $331.0 \text{ cm}^{-1}$  [38], respectively. In addition to those characteristic bands of ZIS and NiTPP, the 15 wt% NiTPP/ZIS heterojunction displays three new emerging ones at  $349.9, 241.5$  and  $223.0 \text{ cm}^{-1}$ , which can be indexed to the Ni-S bonds of NiS [39]. Moreover, the Raman bands in the heterojunction, especially those at *ca.*  $249, 331$  and  $402 \text{ cm}^{-1}$ , are slightly blue-shifts compared to that in the NiTPP and ZIS alone, revealing the intense chemical coupling effect existing between the two components. The FTIR spectra (Fig. S2) show that the NiTPP displays IR bands at  $1439$  and  $694 \text{ cm}^{-1}$ , which can be attributed to the bend and out of plane deformation of C-H in phenyl, while those at  $1068, 790$  and  $1348 \text{ cm}^{-1}$  can be ascribed to the bend, out of plane deformation of C-H and stretching vibrations of C-N in porphyrin [36], respectively. Moreover, the bands located at  $1005$  and  $740 \text{ cm}^{-1}$  are due to the out of plane bending of C-N-Ni bond and N-H in the porphyrin [36]. In comparison with ZIS and NiTPP alone, the NiTPP/ZIS heterojunction shows a new peak at  $619 \text{ cm}^{-1}$ , which can be attributed to Ni-S bond [40]. These results validate that the ZIS and NiTPP components in the heterojunction are combined intimately by Ni-S bonding.

The FESEM images show that the obtained ZIS has floriated microsphere-like morphology with diameters of  $\sim 580 \text{ nm}$  and a hierarchical structure, which is composed by nanosheets with thickness of  $\sim 30 \text{ nm}$  (Fig. 2a,b). These nanosheets in the microspheres can provide large area to contact with NiTPP molecules during the preparation of NiTPP/ZIS heterojunction. The 15 wt% NiTPP/ZIS heterojunction displays a floriated microsphere-like morphology very similar to the ZIS (Fig. 2c,d), suggesting that the refluxing process does not significantly affect the ZIS microstructure. Careful comparison reveals that the surface of microspheres and their nanosheets are decorated with some ultrathin layers (as marked with circles in Fig. 2c,d), which can be further confirmed by the HRTEM images and their fast Fourier transform (FFT) patterns of the ZIS (Fig. 2e) and 15 wt% NiTPP/ZIS heterojunction (Fig. 2f), where certain ultrathin layers are located on those lattice fringes of hexagonal  $ZnIn_2S_4$  as marked with circles in Fig. 2f. Both ZIS and NiTPP/ZIS display clear lattice fringes with a  $d$ -spacing of  $\sim 0.32 \text{ nm}$  (Fig. 2e,f), corresponding to the interfacial spacing of (102) facets of

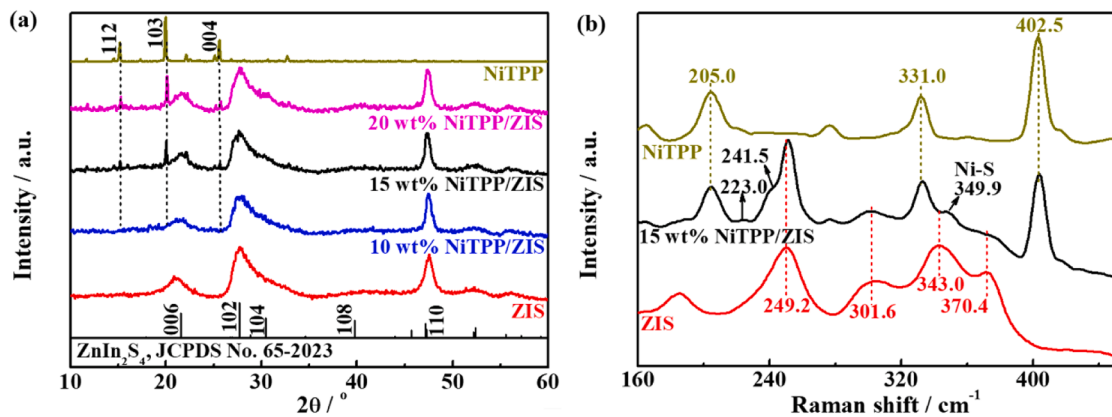


Fig. 1. XRD patterns (a) and Raman spectra (b) of the ZIS, NiTPP and NiTPP/ZIS heterojunctions.

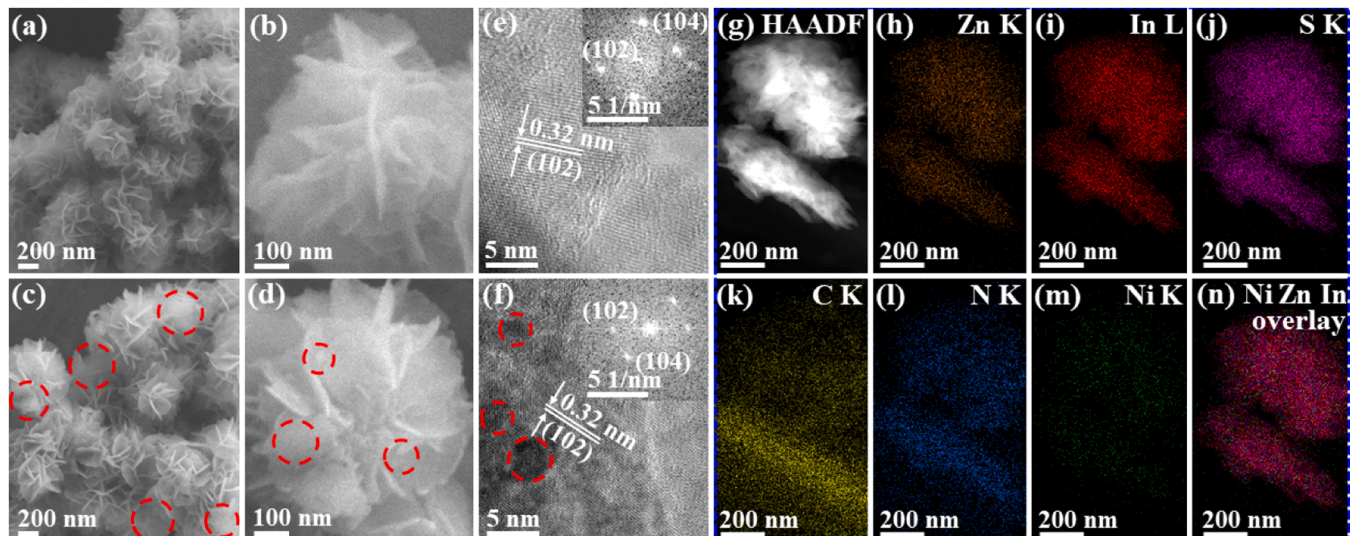


Fig. 2. (a-d) FESEM images of the ZIS (a,b) and 15 wt% NiTPP/ZIS heterojunction (c,d). (e,f) HRTEM images and the corresponding FFT patterns (inset) of the ZIS (e) and 15 wt% NiTPP/ZIS (f). (g-n) HAADF-STEM image (g) and the corresponding EDX Zn (h), In (i), S (j), C (k), N (l), Ni (m) and Ni/Zn/In overlay (n) element mappings of the 15 wt% NiTPP/ZIS heterojunction.

hexagonal ZnIn<sub>2</sub>S<sub>4</sub> [12]. These results suggest that the NiTPP molecules are successfully attached on the hierarchical structure of ZIS microspheres.

The high angle annular dark field-scanning transmission electron microscope (HAADF-STEM) image (Fig. 2g) and its corresponding EDX elemental mappings (Fig. 2h-m) show that the Zn/In/S elements in ZIS and C/N/Zn elements in NiTPP are uniformly distributed in the 15 wt% NiTPP/ZIS particles. The overlay mapping of the Ni/Zn/In elements displays clearly even distribution (Fig. 2n), implying that close contact was built well between the NiTPP and ZIS components. The above results demonstrate that there is uniform NiTPP distribution on the ZIS floriated microspheres. The unique hierarchical structure of NiTPP/ZIS heterojunction not only is beneficial for enhancing the light harvesting *via* reflection and scattering effect between those nanosheets, but also provides large area of close contact between the organic and inorganic components, which is conducive to the formation Ni-S bonding, and then enabling more reactive site and shorted charge diffusion lengths.

### 3.2. Element composition and valence state analyses

The survey X-ray photoelectron spectra (XPS) exhibit that the 15 wt % NiTPP/ZIS heterojunction contains the characteristic binding energy (BE) peaks of Zn, In and S elements, similar to the ZIS (Fig. S3), while the

same BE peaks of C and N elements as the NiTPP can also be observed. There is no obvious BE peak of Ni 2p, possibly due to the low Ni content in the heterojunction. Nevertheless, the elemental analysis and ICP-AES measurement results show that the measured values of C, N and Ni elements in the NiTPP are close to their respective theoretic ones (Table 1), indicating the successful coordination of Ni<sup>2+</sup> ions. Moreover, the measured Zn/In/S (1:2.0:3.9) and C/N/Ni (43.0:3.7:1) atom ratio in the 15 wt% NiTPP/ZIS heterojunction are similar to the elemental

Table 1  
Elemental compositions of the ZIS, NiTPP and 15 wt% NiTPP/ZIS heterojunction.

Sample	ZIS	NiTPP	15 wt% NiTPP/ZIS
Zn (%) <sup>[a]</sup>	15.60 (15.45)	–	13.28 (13.13)
In (%) <sup>[a]</sup>	53.71 (54.29)	–	45.97 (46.15)
S (%) <sup>[a]</sup>	30.69 (30.26)	–	25.53 (25.72)
C (%) <sup>[b]</sup>	–	78.62 (78.71)	12.07 (11.81)
H (%) <sup>[b]</sup>	–	4.25 (4.20)	0.58 (0.63)
N (%) <sup>[b]</sup>	–	8.24 (8.34)	1.20 (1.25)
Ni (%) <sup>[c]</sup>	–	8.89 (8.74)	1.37 (1.31)
Zn/In/S atom ratio	1:2.0:4.0 (1:2:4)	–	1:2.0:3.9
C/N/Ni atom ratio	–	43.2:3.9:1 (44:4:1)	43.0:3.7:1

Data in parentheses are the theoretical contents. <sup>[a]</sup> EPMA, <sup>[b]</sup> EA, <sup>[c]</sup> ICP-AES results.

content ratios in the ZIS (1:2.0:4.0) and NiTPP (43.2:3.9:1), respectively. These results declare that there is no harm to the two components during the preparation process of heterojunction. Based on the Ni contents of 15 wt% NiTPP/ZIS heterojunction, it can be estimated that the NiTPP-loading amount is *ca.* 15.7 wt%, similar to the theoretic one (15.0 wt%) calculated according to the addition amount.

The high-resolution Zn 2p XPS spectra indicate that the ZIS has two obvious BE peaks at 1045.72 and 1022.67 eV (Fig. 3a), attributable to the 2p<sub>1/2</sub> and 2p<sub>3/2</sub> of Zn<sup>2+</sup> species [15], respectively. The In 3d XPS spectrum (Fig. 3b) shows two obvious peaks at 452.83 (In 3d<sub>3/2</sub>) and 445.30 (In 3d<sub>5/2</sub>) eV of In<sup>3+</sup> species [15]. Moreover, the S 2p (Fig. 3c) spectrum can be deconvoluted into two BE peaks at 163.19 (S 2p<sub>1/2</sub>) and 161.95 (S 2p<sub>3/2</sub>) eV [15]. The Zn/In/S elements in 15 wt% NiTPP/ZIS heterojunction shows obvious accumulation of electron density. In detail, the BE values of Zn 2p<sub>1/2</sub> and Zn 2p<sub>3/2</sub> severally shift to 1045.32 and 1022.21 eV, decreasing by *ca.* 0.40 and 0.46 eV (Fig. 3a), while the

ones of In 3d<sub>3/2</sub>/3d<sub>5/2</sub> and S 2p<sub>1/2</sub>/2p<sub>3/2</sub> present negative shifts of *ca.* 0.30/0.31 and 0.50/0.37 eV (Fig. 3b,c), respectively. These results validate that the ZIS has considerable potential to collect electrons after coupled with NiTPP.

In contrast, the BE values of C 1s (Fig. 3d), N 1s (Fig. 3e), Ni 2p<sub>1/2</sub> and Ni 2p<sub>3/2</sub> (Fig. 3f) for the 15 wt% NiTPP/ZIS heterojunction signify positive shifts compared with those of the NiTPP alone. Specially, the high-resolution C 1s spectrum (Fig. 3d) of NiTPP can be divided into two peaks belonged to C-N (286.02 eV) and C-C/C=C (284.60 eV) [17,41]. After compounding with the ZIS, the BE value of conjugated structure C-C/C=C remains unchanged, while that of C in C-N bonds positively shifts to 286.12 eV, implying that there is a decreased electron cloud density of C in the C-N bonds. As for the single NiTPP, the high-resolution N 1s peak located at 398.50 eV is due to N-Ni bond of the metalloporphyrin (Fig. 3e), which clearly shifts to 398.60 eV after combining with ZIS. The NiTPP alone exhibits two intense XPS peaks at

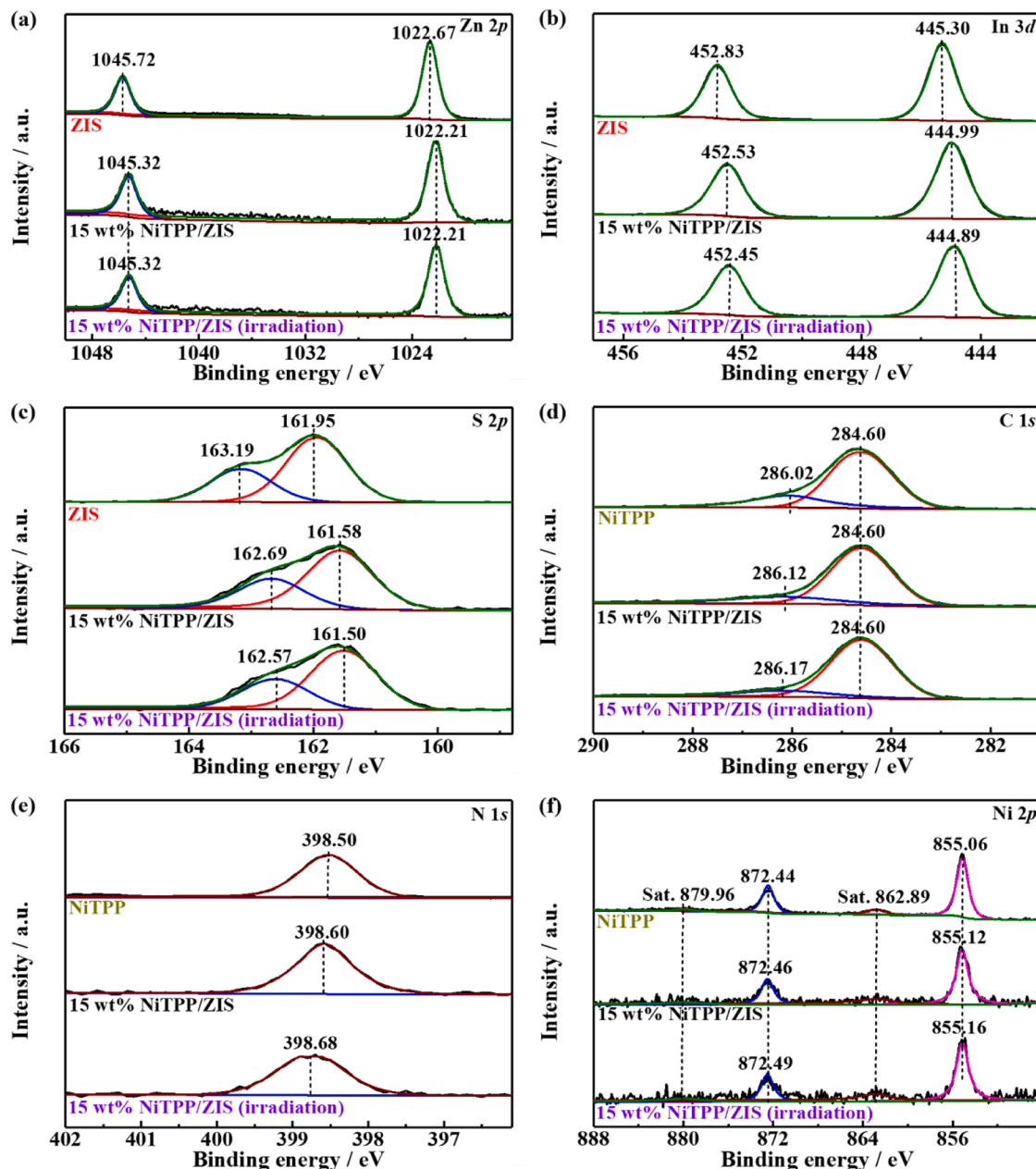


Fig. 3. High-resolution Zn 2p (a), In 3d (b), S 2p (c), C 1s (d), N 1s (e) and Ni 2p (f) XPS spectra of the ZIS, NiTPP and 15 wt% NiTPP/ZIS heterojunction as well as the 15 wt% NiTPP/ZIS heterojunction after illumination for 15 min.

872.44 and 855.06 eV along with two weak ones at 879.96 and 862.89 eV (Fig. 3f), which is attributed to the Ni  $2p_{1/2}$  and Ni  $2p_{3/2}$  and their satellite peaks [31], respectively. Likewise, the bonding energy values of Ni  $2p_{1/2}/2p_{3/2}$  peaks in the 15 wt% NiTPP/ZIS heterojunction increase by *ca.* 0.02/0.06 eV, up to 872.46/855.12 eV, these less increases in the electron cloud density of the porphyrin Ni in comparison with the C and N elements may be ascribed to its electron-rich environment provided by ligand N atoms and the porphyrin ring of the conjugated structure, that is, there is ligand to metal charge transfer (LMCT) process in the NiTPP [42].

The above shifts of BE peaks for C, N and Ni atoms in the NiTPP after coupling with ZIS suggest that the electrons will flow from C to N atoms, and then to the Ni<sup>2+</sup> center *via* LMCT process. Moreover, those distinct binding energy differences of Zn/In/S and C/N/Ni atoms between the 15 wt% NiTPP/ZIS heterojunction and its components also give a strong evidence that an intense chemical coupling effect happens to the ZIS and NiTPP components, where ZIS serving as an electron enrichment reservoir accepts electrons from NiTPP that act as an electron donor *via* the Ni-S bonds formed between the two components as mentioned above, which will be beneficial for boosting the photoactivity for H<sub>2</sub> production as demonstrated below.

### 3.3. Photocatalytic activity and stability analyses

The photoreaction conditions with the 15 wt% NiTPP/ZIS heterojunction as catalyst for H<sub>2</sub> evolution reaction were optimized initially under visible light ( $\lambda \geq 400$  nm) irradiation. Among those commonly used electron donors such as methanol (CH<sub>3</sub>OH), ascorbic acid (AA), triethanolamine (TEOA), disodium ethylenediamine tetraacetic acid (EDTA) and Na<sub>2</sub>S+Na<sub>2</sub>S<sub>2</sub>O<sub>3</sub>, TEOA leads to the best H<sub>2</sub> evolution activity (Fig. S4a). The 15 wt% NiTPP/ZIS heterojunction delivers obviously

increased H<sub>2</sub> evolution activity along with enhancing the TEOA concentration from 5.0 vol% to 15 vol%, and then slightly decrease after further enhancing the TEOA concentration to higher than 15 vol% (Fig. S4b). Besides, the 15 wt% NiTPP/ZIS heterojunction with 15 vol% TEOA as electron donor exhibits a gradually increased H<sub>2</sub> evolution activity with the enhancement of catalyst dosage from 40 to 80 mg, and then a slightly decreased activity was obtained when the catalyst dosage rises to 90 mg (Fig. S4c). Therefore, the photoreaction conditions for the 15 wt% NiTPP/ZIS heterojunction are optimized as 80 mg catalyst in 50 mL of 15 vol% TEOA solution under visible light ( $\lambda \geq 400$  nm) irradiation.

Under the optimal photoreaction conditions, the effect of the NiTPP-loading amount on the photoactivity of the NiTPP/ZIS heterojunction was further investigated under visible light ( $\lambda \geq 400$  nm) irradiation. As seen from Fig. 4a, the H<sub>2</sub> evolution activity is markedly boosted along with enhancing the NiTPP-loading amount from 5 wt% to 15 wt%, and then decreased upon further enhancing the NiTPP-loading to higher than 15 wt%. Namely, the 15 wt% NiTPP/ZIS heterojunction presents an optimal H<sub>2</sub> evolution activity of 2305  $\mu\text{mol h}^{-1}$ , 10 and 256 times higher than that of the ZIS (229  $\mu\text{mol h}^{-1}$ ) and NiTPP (9.0  $\mu\text{mol h}^{-1}$ ) alone, respectively. It indicates that the combination of NiTPP and ZIS components can greatly boost the photoactivity for H<sub>2</sub> production.

The long-term photoreaction experiments for H<sub>2</sub> evolution were further conducted as shown in Fig. 4b. During the four consecutive runs, the photoreaction system was evacuated for every hour assessment of H<sub>2</sub> yield and then *ca.* 1 mL of 15 vol% TEOA solution was added for the next hour photocatalytic test. The photocatalytic performance of the 15 wt% NiTPP/ZIS heterojunction under visible light ( $\lambda \geq 400$  nm) irradiation was basically unchanged during the 20 h of four consecutive cycles, and exhibited a nearly straight line relationship with no significant deactivation occurred. For instance, an average H<sub>2</sub> evolution activity of 2251

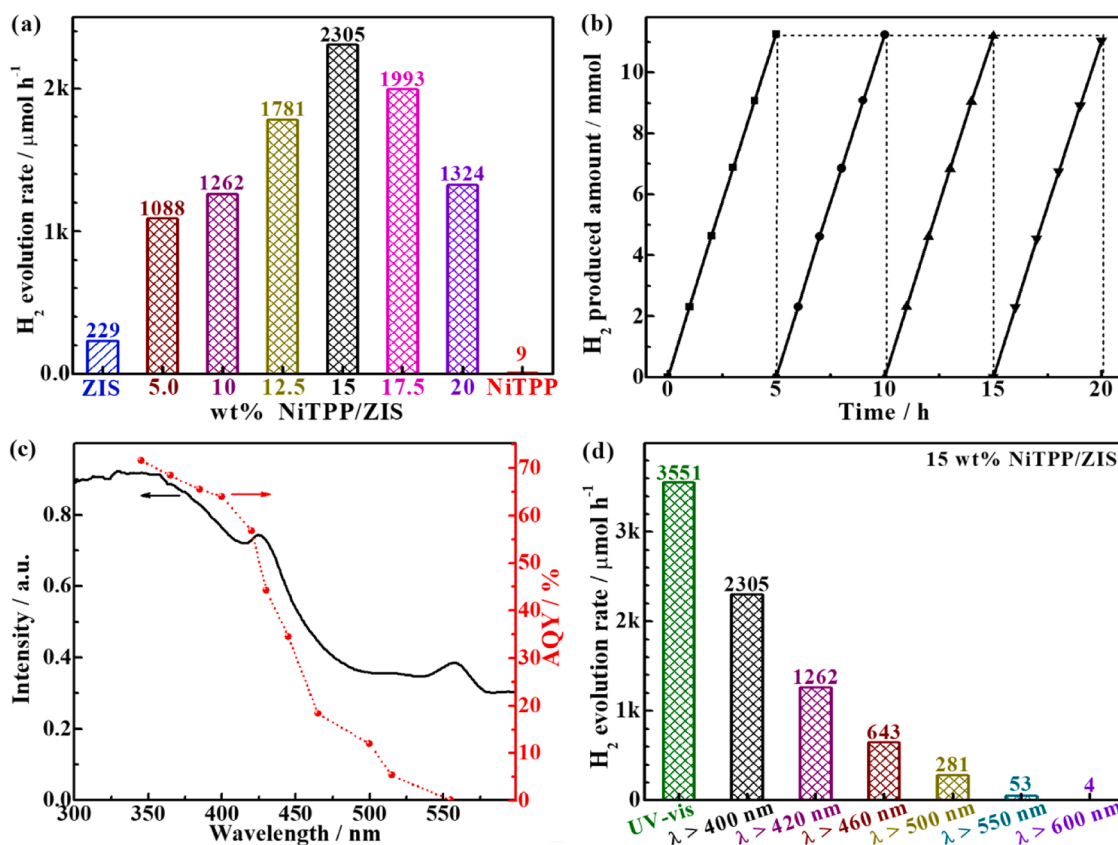


Fig. 4. (a) Effect of the NiTPP-loading amount on the H<sub>2</sub> evolution activity of the NiTPP/ZIS heterojunction. (b) Time courses for the H<sub>2</sub> evolution over the 15 wt% NiTPP/ZIS heterojunction. (c) Wavelength-dependent AQY curve for the H<sub>2</sub> evolution over the 15 wt% NiTPP/ZIS heterojunction. (d) Effect of the incident spectral region on the H<sub>2</sub> evolution activity of the 15 wt% NiTPP/ZIS heterojunction. Conditions: 80 mg catalyst in 50 mL of 15 vol% TEOA solution unless otherwise stated.

$\mu\text{mol h}^{-1}$  is obtained in the first run, which just decreased by 0.04 %, 0.44 % and 1.87 % in the second (2250  $\mu\text{mol h}^{-1}$ ), third (2241  $\mu\text{mol h}^{-1}$ ) and fourth (2209  $\mu\text{mol h}^{-1}$ ) runs, respectively. Furthermore, the recovered catalyst after the 20 h photoreaction remains nearly unchanged features in morphology (Fig. S5), crystal phase (Fig. S6a), FTIR (Fig. S6b) and XPS (Fig. S7) spectra. The above results demonstrate that the NiTPP/ZIS heterojunction has superior photoactivity and stability under the present photoreaction conditions.

Under monochromatic light irradiation of 345, 365, 385, 400, 420, 445, 465, 500, 515 and 555 nm, the 15 wt% NiTPP/ZIS heterojunction delivers apparent quantum yields (AQY) up to 71.7 %, 68.4 %, 65.5 %, 64.0 %, 56.8 %, 34.6 %, 18.3 %, 11.9 %, 5.4 % and 0.1 % (Fig. 4c), respectively. The corresponding changing tendency is basically consistent with the light absorption curve in the range of 350–550 nm, revealing the light excitation of catalyst is the driving force of  $\text{H}_2$  production in the photoreaction system. Those spectral absorption longer than 560 nm of the heterojunction seems not to contribute  $\text{H}_2$  production, which can be further confirmed by the  $\text{H}_2$  evolution activity of the 15 wt% NiTPP/ZIS heterojunction under different spectral region. As seen from Fig. 4d, the heterojunction shows a very low activity of 4.0  $\mu\text{mol h}^{-1}$  under  $\lambda \geq 600$  nm light irradiation. It may be ascribed to this long wavelength responsive feature of the heterojunction contributed by the decorated NiTPP with very low activity (Fig. 4a).

Along with enlarging the wavelength region, the activity displays an obvious increasing trend. For instance, the  $\text{H}_2$  evolution activity is 53, 281, 643, 1262, 2305  $\mu\text{mol h}^{-1}$  under  $\lambda \geq 550$ , 500, 460, 420 and 400 nm light irradiation, respectively. Especially, the 15 wt% NiTPP/ZIS heterojunction delivers an ultrahigh  $\text{H}_2$  evolution activity of 3551  $\mu\text{mol h}^{-1}$  under full spectrum irradiation of Xe-lamp (Fig. 4d). These photocatalytic  $\text{H}_2$  evolution performance with remarkable  $\text{H}_2$  evolution activity of 2305 and 3551  $\mu\text{mol h}^{-1}$  under visible light ( $\lambda \geq 400$  nm) and

full spectrum irradiation of Xe-lamp as well as superior AQY of 64.0 % at 400 nm and 56.8 % at 420 nm are much better than that of most  $\text{ZnIn}_2\text{S}_4$ -based or porphyrin-based photocatalytic systems reported previously (Table S1) [12–16, 18, 22, 25, 26, 29, 30], suggesting that the present NiTPP/ZIS heterojunction would be a commendable photocatalyst for manufacturing artificial photosynthesis with light-to-chemical energy conversion.

### 3.4. Survey on the photocatalytic mechanism

To explore the performance enhancement mechanism of the NiTPP/ZIS heterojunction, its optical absorption property and energy band structure were investigated initially. The UV-vis diffuse reflectance absorption spectra (DRS) indicate that the NiTPP displays much wide solid-state absorption from UV through the visible region up to 800 nm than the NiTPP in DMF solution (Fig. 5a). Instead of four Q bands of free-based porphyrin, the only one Q-band absorption peak of NiTPP in DMF solution is due to high symmetry of metalized porphyrin [43], while the solid-state absorption of NiTPP is more complex than that in solution, implying that the molecular aggregation state significantly affects the optical absorption property of NiTPP [44]. On the other hand, the ZIS alone exhibits a solid-state absorption spectrum with an onset wavelength of  $\sim 515$  nm, while the 15 wt% NiTPP/ZIS heterojunction shows the combined features of ZIS and NiTPP with the DRS spectra extend to longer wavelength, which can be attributed to the enhancement of the surface electric charge of ZIS component in the heterojunction due to the co-existed NiTPP, because NiTPP has strong visible absorption (upper section in Fig. 5a), which may lead to modification of the charge carrier generation process [27]. Meanwhile, the B- and Q-band absorptions of NiTPP in the heterojunction exhibit *ca.* 13 and 22 nm redshift compared with the NiTPP solution, it may be due to the interaction between NiTPP

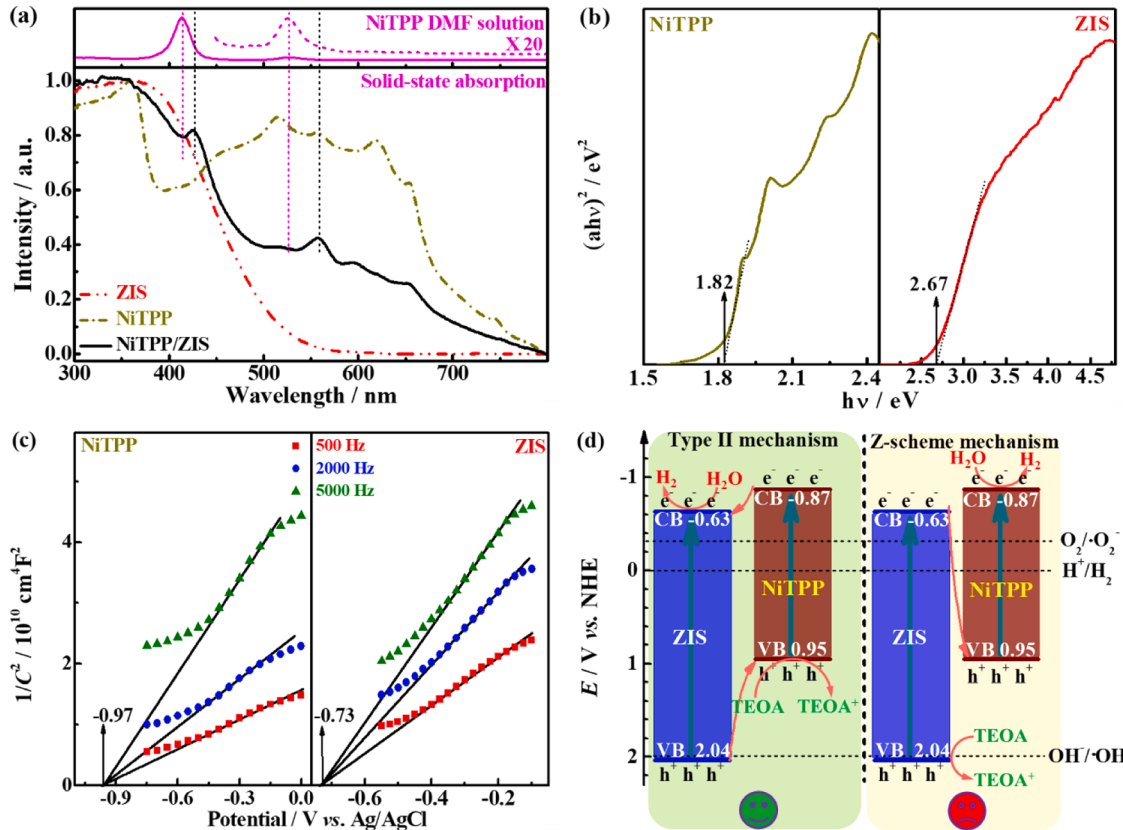


Fig. 5. (a) UV-vis diffuse reflectance absorption spectra (DRS) of the ZIS, NiTPP and 15 wt% NiTPP/ZIS heterojunction and UV-vis absorption spectra of the NiTPP DMF solution. (b) Tauc plots of the ZIS and NiTPP. (c) Mott-Schottky M-S curves of the NiTPP and ZIS. (d) Energy band structures and the possible photocatalytic mechanisms of the NiTPP/ZIS heterojunction.

and ZIS components, that is, the Ni-S bonding formed between the two components as mentioned above.

Since it was reported that  $\text{ZnIn}_2\text{S}_4$  is a direct bandgap semiconductor [26], the optical bandgap energy ( $E_g$ ) of ZIS can be calculated as  $\sim 2.67$  eV using the Tauc plots (Fig. 5b) derived from its DRS spectra. Similarly, the  $E_g$  of NiTPP can be estimated as 1.82 eV, consistent with the result derived from the normalized absorption and emission spectra (Fig. S8a) of the NiTPP DMF solution, whereby the bandgap energy ( $E_{0-0}$ ) of NiTPP can be estimated as  $\sim 1.78$  eV based on the equation of  $E_{0-0} = 1240/\lambda_{\text{int}}$  ( $\lambda_{\text{int}}$  = the intersection point at  $\sim 696$  nm of the two curves). It is depicted in Fig. 5c that the Mott-Schottky curves of ZIS and NiTPP show positive slopes, suggesting that both of them are n-type semiconductor. The intercepts of ZIS and NiTPP with x-axis are  $-0.73$  and  $-0.97$  V vs. Ag/AgCl (saturated KCl solution,  $E = 0.198$  V vs. NHE), and thus their flat band potentials ( $E_{\text{fb}}$ ) are estimated as  $-0.73$  and  $-0.97$  V vs. Ag/AgCl, respectively. Since the conduction band minimum ( $E_{\text{CB}}$ ) is usually 0.10 V more negative than  $E_{\text{fb}}$  for n-type semiconductor [45], the  $E_{\text{CB}}$  of ZIS and NiTPP can be calculated as  $-0.63$  ( $= -0.73 + 0.198 - 0.10$ ) V vs. NHE and  $-0.87$  V vs. NHE, respectively.

Based on the equation ( $E_{\text{VB}} = E_g + E_{\text{CB}}$ ), the valence band maximum ( $E_{\text{VB}}$ ) of NiTPP and ZIS are calculated as 0.95 and 2.04 V vs. NHE, respectively. According to the cyclic voltammetry (CV) curves (Fig. S8b), the  $E_{\text{ox}}$  of NiTPP in DMF solution is calculated to be  $+0.94$  V vs. NHE by using the equation of  $E_{\text{ox}}$  (vs. NHE) =  $E_{\text{ox}}$  (vs. Ag/AgCl) -  $E_1/2$  ( $\text{Fc}^+/\text{Fe}$  vs. Ag/AgCl) +  $E_1/2$  ( $\text{Fc}^+/\text{Fe}$  vs. NHE) [9], well in accord with the  $E_{\text{VB}}$  of NiTPP. Therefore, the schematic band structure diagram of the NiTPP/ZIS heterojunction can be drawn as Fig. 5d. Accordingly, both of the two components in the heterojunction can satisfy with the thermodynamic energy criterion for  $\text{H}_2$  evolution reaction, thus two possible mechanisms are proposed. One is Z-scheme heterojunction and the other

is II-type heterojunction as shown in Fig. 5d. As mentioned above, the bare NiTPP just displays negligible activity of  $9.0 \mu\text{mol h}^{-1}$ , the ZIS alone delivers a  $\text{H}_2$  evolution activity of  $229 \mu\text{mol h}^{-1}$ , while the NiTPP/ZIS heterojunction gives a markedly boosted  $\text{H}_2$  evolution activity ( $2305 \mu\text{mol h}^{-1}$ ), 9.6 times higher than the sum activity ( $238 \mu\text{mol h}^{-1}$ ) of the NiTPP and ZIS alone (Fig. 4a). It suggests that there exists significant synergistic effect between the two components, and the ZIS may act as the main component for  $\text{H}_2$  evolution reaction.

The above conjecture can be further validated by the comparative experiments conducted under the optimized photoreaction conditions. As shown in Fig. 6a, the physical mixture (NiTPP+ZIS) with the same mass ratio just shows an activity of  $824 \mu\text{mol h}^{-1}$ , much lower than that of the NiTPP/ZIS heterojunction, and there is a huge difference in the activities between the NiTPP/ZIS ( $339 \mu\text{mol h}^{-1}$ ) and NiTPP/ZIS heterojunction. These results highlight that the significantly boosted charge separation and transfer efficiency may be possibly ascribed to the Ni-S highway formed between the two components as mentioned above. Besides, 1.0 wt% Pt as a cocatalyst brings obvious enhancement in the  $\text{H}_2$  evolution performance of those control catalysts except for the (Pt-NiTPP)/ZIS (Fig. 6a). It implies that the ZIS but not the NiTPP component in the heterojunction would be the  $\text{H}_2$ -evolving component, and thus a type II charge transfer mechanism would proceed in the heterojunction as shown in Fig. 5d. A direct evidence of this conjecture can be obtained from Fig. 6a, whereby the NiTPP/(Pt-ZIS) heterojunction with Pt-loading on ZIS displays a much higher  $\text{H}_2$  evolution activity ( $2838 \mu\text{mol h}^{-1}$ ) than that ( $2305 \mu\text{mol h}^{-1}$ ) of the NiTPP/ZIS heterojunction without Pt-loading under visible light irradiation, while the (Pt-NiTPP)/ZIS heterojunction with Pt-loading on the NiTPP exhibits a slightly lower activity ( $2235 \mu\text{mol h}^{-1}$ ) than the NiTPP/ZIS heterojunction. It means that those Pt nanoparticles loaded on the NiTPP would retard the

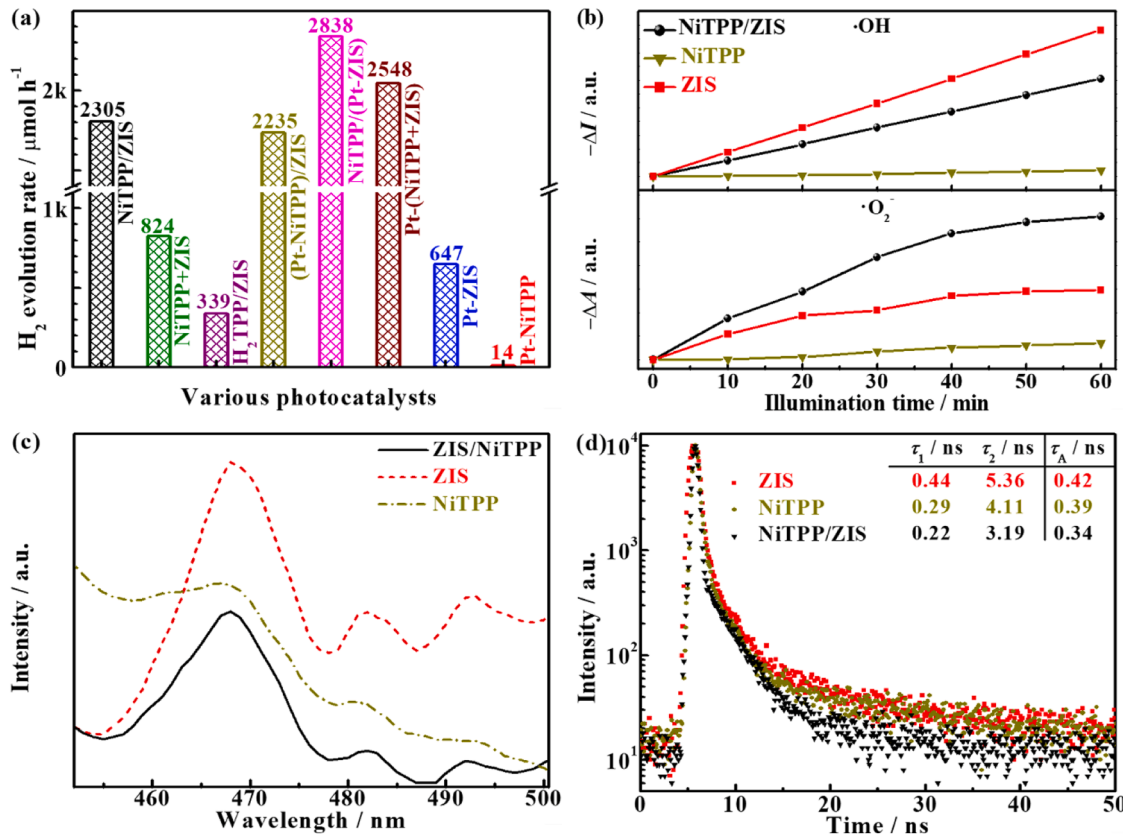


Fig. 6. (a) Comparison of the  $\text{H}_2$  evolution activity over various catalysts. Conditions: 80 mg catalyst in 50 mL of 15 vol% TEOA solution under visible light ( $\lambda = 400$  nm) irradiation. (b) Absorbance decrease ( $-\Delta A$ ) of the NBT solution at 259 nm (bottom) and fluorescence enhancement ( $+\Delta I$ ) of the TA solution at 431 nm (up) along with the irradiation time. (c) Steady-state photoluminescence (PL) spectra of the ZIS, NiTPP and 15 wt% NiTPP/ZIS heterojunction. (d) Time-resolved fluorescence decay (TRFS) spectra of the ZIS, NiTPP and 15 wt% NiTPP/ZIS heterojunction with  $\lambda_{\text{ex}} = 375$  nm and  $\lambda_{\text{em}} = 469$  nm.

photoexcited electrons transferring from the NiTPP to ZIS component for H<sub>2</sub> evolution. These results confirm the ZIS component as the electron-rich reservoir is responsible for the H<sub>2</sub> evolution reaction through a type II heterojunction mechanism.

To give more direct evidence, *in situ* high-resolution XPS spectra under full spectrum irradiation of Xe-lamp for 15 min (Fig. 3) are applied to figure out which charge transfer mechanism the NiTPP/ZIS heterojunction belongs to. Under irradiation, the BE values of Zn 2p<sub>1/2</sub>/2p<sub>3/2</sub> of NiTPP/ZIS (Fig. 3a) remained unchanged as those of ex situ XPS spectra. However, the XPS peaks of In 3d<sub>3/2</sub>/In 3d<sub>5/2</sub> (Fig. 3b) are severely reduced to 452.45/444.89 eV, showing a dent of *ca.* 0.08/0.10 eV in contrast with those before illumination. Similarly, the BE values of the S 2p<sub>1/2</sub>/2p<sub>3/2</sub> (Fig. 3c) for NiTPP/ZIS heterojunction after the illumination drop from 162.69/161.58 eV to 162.57/161.50 eV, the 0.12/0.08 eV declines demonstrate the increased electron cloud density of ZIS component in the NiTPP/ZIS heterojunction.

The above results validate the magnitude trend of electron flow to ZIS, and the relative intensity of binding energy drops indicate that the ZIS component may receive electrons through S<sup>2-</sup>, and that the electrons then transfer to nearby In<sup>3+</sup> species. In contrast, under irradiation, the BE peak of C-N bond of NiTPP in the NiTPP/ZIS heterojunction shifts to 286.17 eV (Fig. 3d), increasing by *ca.* 0.05 eV. And the binding energy of N 1s rises to 398.68 eV (Fig. 3e), while the BE values of Ni 2p<sub>1/2</sub>/2p<sub>3/2</sub> increase by *ca.* 0.03/0.04 eV to 872.49/855.16 eV compared to those of ex situ XPS (Fig. 3f), respectively. These opposite XPS behaviors on the ZIS and NiTPP components after the irradiation clearly exhibit that the electrons would flow from the NiTPP to ZIS components for H<sub>2</sub> evolution reaction *via* type II heterojunction mechanism. Based on the above results and discussion, it can be speculated that TEOA as sacrificial reagent would rapidly consume the photogenerated holes of the NiTPP component, and the corresponding photoexcited electrons in the NiTPP would transfer to the ZIS components. In detail, the conjugated structure in the porphyrin can quickly accept the electrons from the TEOA molecules that react with the photoexcited holes in the NiTPP component, while the Ni<sup>2+</sup> center of porphyrin as a transition station instantly inject those electrons to the ZIS component through the Ni-S highway as soon as it absorbs the remain photoexcited electrons through C-N and N-Ni bonds. Finally, electrons accumulate on ZIS and participate in the H<sub>2</sub> evolution reaction.

The proposed inner charge transfer pathway can be further validated by the superoxide radical (•O<sub>2</sub><sup>-</sup>) and hydroxyl radical (•OH) quantification experiments using nitroblue tetrazolium (NBT) and terephthalic acid (TA) as probe molecules [35]. The decrease in absorbance (-ΔA, at 259 nm) along with the irradiation time can be calculated from those UV-Vis absorption spectra of NBT solutions containing various catalysts (Fig. S9). As seen from Fig. 6b, the NiTPP alone shows sluggish reduction kinetics from O<sub>2</sub> to •O<sub>2</sub><sup>-</sup> compared with the ZIS even though both of them meet the thermodynamic requirement of O<sub>2</sub> to •O<sub>2</sub><sup>-</sup> ( $E^\theta = -0.33$  V *vs.* NHE [35] as shown in Fig. 5d). It agrees with the above results on the higher H<sub>2</sub> evolution activity of ZIS than NiTPP, suggesting that the ZIS serves as the superior H<sub>2</sub>-evolving unit in the heterojunction. Besides, the fastest kinetics for the NiTPP/ZIS heterojunction exhibits the great advantage of type II heterojunction for the charge separation. On the other hand, the enhancement in the fluorescence ( $\Delta I$ , at 431 nm) of TA solutions containing various catalysts can be estimated from the fluorescence spectra (Fig. S10). The NiTPP alone under irradiation cannot lead to any obvious fluorescence enhancement (Fig. 6b), owing to the thermodynamically unfavorable to the •OH generation since the  $E_{VB}$  (0.95 V *vs.* NHE) is more negative than H<sub>2</sub>O/•OH potential ( $E^\theta = 1.99$  V *vs.* NHE, Fig. 5d) [5], while the single ZIS quickly generated numerous •OH species due to the more positive  $E_{VB}$  than H<sub>2</sub>O/•OH potential. In contrast with the single ZIS, the relatively slower OH<sup>-</sup> to •OH oxidation kinetics for the heterojunction also does not support a Z-scheme mechanism, but implies an excellent hole transfer efficiency from ZIS to NiTPP component in the type II heterojunction.

The effective charge transfer and separation through the Ni-S

bonding in the heterojunction can be further verified by the photoluminescence (PL, Fig. 6c) spectra. After excitation, the single ZIS shows obvious strong fluorescence signal at *ca.* 468 nm, and the NiTPP alone has much lower signal, while the heterojunction displays markedly reduced PL emission intensity than the ZIS and NiTPP. It demonstrates that the coupling of NiTPP with ZIS can efficiently retard the photoinduced charge recombination due to holes in the ZIS component transferring towards the NiTPP effectively stemmed from their intimate interfacial contact and the Ni-S bonding. Time-resolved fluorescence spectra (TRFS, Fig. 6d) were applied to further detect the carrier dynamics. The average fluorescence lifetime was calculated according to equation of  $\tau_A = (A_1\tau_1^2 + A_2\tau_2^2)/(A_1\tau_1 + A_2\tau_2)$ , where  $\tau_1$  is generated by the nonradiative recombination of charge carriers,  $\tau_2$  is caused by the radiative recombination of free excitons [46], and their amplitudes are represented by A<sub>1</sub> and A<sub>2</sub> (Table. S2), respectively. The NiTPP/ZIS heterojunction exhibits the shorter  $\tau_1$  but larger percentage (A<sub>1</sub>) than the single ZIS, suggesting a more efficient photoinduced electron transfer from NiTPP to ZIS [47]. The corresponding fitted values show that the ZIS has much longer electron lifetime (0.42 ns) than the NiTPP (0.39 ns). However, the photogenerated electrons of the NiTPP/ZIS heterojunction has an average lifetime of 0.34 ns, suggesting that the Ni-S channel can act as a highway to promote the photogenerated charge separation of the ZIS component, and thus efficiently shorten the fluorescence lifetime. These results of charge carrier migration dynamics indicated that the synergistic effect of ZIS and NiTPP components greatly boosted the separation of photogenerated electrons and holes, which is beneficial to enhance the H<sub>2</sub> production performance.

The physicochemical and photoelectrochemical characterization are subsequently implemented to further explore the underlying performance enhancement mechanism of the heterojunction. The electrochemical impedance spectra (EIS, Fig. 7a) reveal the interface charge transfer impedance ( $R_{ct}$ ), whereby the smaller radius of curve represents the smoother interface charge transfer with a lower  $R_{ct}$  value [5]. The single NiTPP exhibits the largest arc radius, indicating its poor conductivity, while the NiTPP/ZIS heterojunction presents much smaller  $R_{ct}$  (8.3 kΩ) than ZIS (20.6 kΩ) and NiTPP (97.1 kΩ) alone, suggesting its much faster interfacial charge transfer. Moreover, the H<sub>2</sub>TPP/ZIS heterojunction displays a higher  $R_{ct}$  (51.3 kΩ) than the NiTPP/ZIS heterojunction, suggesting its strong interfacial charge resistance, which is consistent with their H<sub>2</sub> evolution activities (Fig. 6a). Similarly, the enhanced charge separation can be verified by the photocurrent curves (Fig. 7b). The NiTPP/ZIS heterojunction possesses the highest photocurrent density, while the ZIS alone exhibits the lowest one, and the NiTPP show suboptimal photocurrent response. These results indicate that the NiTPP in the heterojunction plays a significant role in the enhancements of charge transfer efficiency and photoactivity. Notably, those catalysts containing NiTPP show the “spike” feature or a decay tendency in the photocurrent (Fig. 7b), which is associated with the charge separation and recombination [48]. Compared with the single NiTPP, the weakening of the transient photocurrent spike of the heterojunction demonstrates that the holes generated from the NiTPP can be quickly consumed by the electron donor (H<sub>2</sub>O) with the aid of ZIS.

Based on those on-off photocurrent decay curves, a normal parameter D can be calculated with the equation of  $D = (I_t - I_{st})/(I_{in} - I_{st})$ , where  $I_t$ ,  $I_{st}$ , and  $I_{in}$  are the time-dependent current, the stable-state current at  $t \rightarrow \infty$ , and the initial transient peak current as shown in Fig. S11 [48], respectively. Therefore, the lnD-t plots of those catalyst can be drawn as shown in Fig. 7c. To quantify the charge recombination rate, the transient time constant ( $k$ ), worked as a figure-of-merit appraising general behavior of charge recombination, is equal to the time variable at which lnD = -1 in the lnD-t plots [48,49]. Obviously, the  $k$  values of the NiTPP, H<sub>2</sub>TPP/ZIS and NiTPP/ZIS are calculated to be 0.94, 1.08 and 1.54 s, respectively. It validates the most efficient charge separation in the NiTPP/ZIS heterojunction and the considerable effect of Ni-S bonding on the charge transfer process.

To further explore how transferability is improved, the

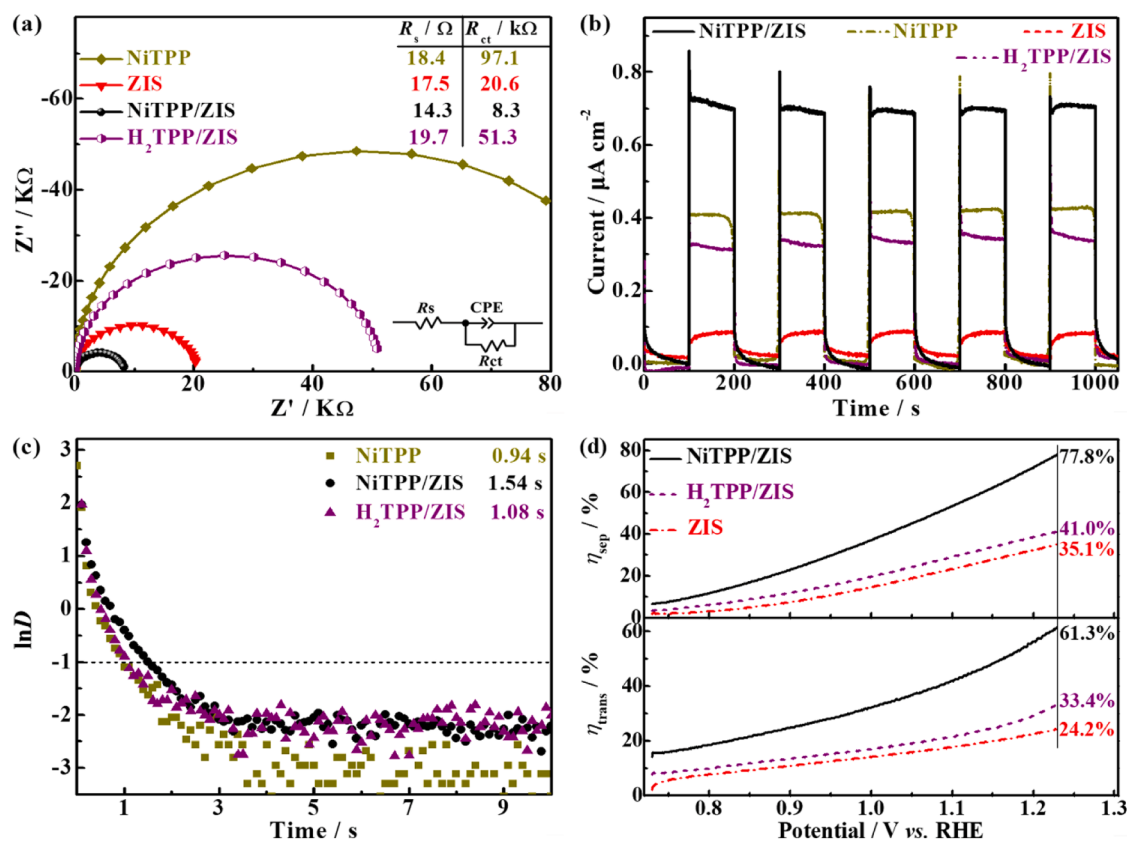


**Fig. 7.** (a) EIS spectra of the ZIS, NiTPP and 15 wt% NiTPP/ZIS and H<sub>2</sub>TPP/ZIS heterojunctions. (b) Transient photocurrent response curves of the ZIS, NiTPP, 15 wt% H<sub>2</sub>TPP/ZIS and NiTPP/ZIS heterojunctions. (c) Transient time constant derived from the on-off photocurrent decay curves in (b). (d) Photogenerated charge separation efficiency ( $\eta_{sep}$ , up) and charge transfer efficiency ( $\eta_{trans}$ , bottom) curves of the ZIS, 15 wt% H<sub>2</sub>TPP/ZIS and NiTPP/ZIS heterojunctions.

photogenerated charge separation efficiency ( $\eta_{sep}$ ) and charge transfer efficiency ( $\eta_{trans}$ ) of those ZnIn<sub>2</sub>S<sub>4</sub>-based catalysts are investigated based on those photocurrent curves with Na<sub>2</sub>SO<sub>3</sub> solution (as hole scavenger) and the photocurrent curves in deionized water (without hole scavenger) under AM1.5 G illumination as shown in Fig. S12 [32,33]. The single ZIS displays a  $\eta_{sep}$  of 35.1 % and  $\eta_{trans}$  of 24.2 % at 1.23 V (Fig. 7d). Although the H<sub>2</sub>TPP/ZIS heterojunction exhibits much improved  $\eta_{sep}$  (41.0 %) and  $\eta_{trans}$  (33.4 %) at 1.23 V, the NiTPP component in the NiTPP/ZIS heterojunction takes much more obvious effect, and brings the  $\eta_{sep}$  and  $\eta_{trans}$  up to 77.8 % and 61.3 % at 1.23 V, respectively. These results reveal that the Ni-S bonds in the NiTPP/ZIS heterojunction may serve as a charge transfer highway between the two components, making a remarkable contribution to the improvement in charge separation/transfer and photocatalytic performance.

On the bases of the above results and discussion, a novel nickel porphyrin/ZnIn<sub>2</sub>S<sub>4</sub> heterojunction with Ni-S highway and high-efficient type II photocatalytic mechanism is fabricated for boosting charge separation and visible-light-driven H<sub>2</sub> production. With no need of cocatalyst, the NiTPP/ZIS heterojunction delivers a remarkable H<sub>2</sub> evolution activity of 2305  $\mu\text{mol h}^{-1}$  under visible light ( $\lambda \geq 400 \text{ nm}$ ) with superior AQYs up to 64.0 % (at 400 nm) and 56.8 % (at 420 nm). Further investigations demonstrate that the resultant NiTPP/ZIS exhibits enhanced optical absorption, charge separation and photoelectrochemical behavior compared with the NiTPP and ZIS alone, which can be ascribed to the synergy of the type II heterojunction charge transfer mechanism and the Ni-S channel, and thus enabling the high photoactivity and durability. The results presented here validate that the NiTPP/ZIS heterojunction would be a commendable organic-inorganic hybrid photocatalyst for manufacturing artificial photosynthesis with highly efficient light-to-chemical energy conversion.

#### 4. Conclusions

In summary, a novel organic-inorganic hybrid heterojunction (NiTPP/ZnIn<sub>2</sub>S<sub>4</sub>) was fabricated using NiTPP and ZIS as raw materials through a facile reflux process. It was found that the interfacial Ni-S bonds act as charge transfer highway between the NiTPP and ZIS components, realizing remarkable photocatalytic activity and stability for H<sub>2</sub> evolution reaction. The large contact area and Ni-S intense chemical coupling effect provide necessary driving force steering the photogenerated electrons transferring to the ZIS units with fast holes consumption kinetics following a type II heterojunction mechanism. What's more, the porphyrin with narrow  $E_g$  contributes to the enhanced light absorption, while the ZIS component provides high active sites, the combination of NiTPP and ZIS brings out accelerated photoinduced charge separation and transfer. The above factors synergistically lead to significant improvements of photocatalytic performance, specially, the NiTPP/ZIS heterojunction exhibits a remarkable H<sub>2</sub> evolution activity of 2305  $\mu\text{mol h}^{-1}$  under visible light ( $\lambda \geq 400 \text{ nm}$ ) irradiation with superior AQYs up to 64.0 % (at 400 nm) and 56.8 % (at 420 nm). The present study not only provides an efficient strategy for constructing heterojunction with Ni-S channel to boost the charge carrier mobility and H<sub>2</sub> production, but also presents a novel concept to fabricate porphyrin-contained high-performance artificial photosynthetic system of inorganic-organic hybrid materials.

#### CRediT authorship contribution statement

**Renjie Li:** Funding acquisition, Conceptualization. **Tianyou Peng:** Writing – review & editing, Visualization, Supervision, Project administration, Funding acquisition. **Huaiyang Jia:** Writing – original draft, Visualization, Methodology, Investigation, Conceptualization. **Xinxin**

**Shao:** Validation, Investigation, Data curation. **Ya'nan Wang:** Investigation, Data curation. **Jing Zhang:** Methodology, Conceptualization.

## Declaration of Competing Interest

The authors declare that they have no known competing financial interests or personal relationships that could have appeared to influence the work reported in this paper.

## Data availability

Data will be made available on request.

## Acknowledgments

This work was supported by the National Natural Science Foundation of China (22372123, 22271223 and 21975190), and the Science and Technology Planning Project of Shenzhen Municipality (CN) (JCYJ20180302153921190), China.

## Appendix A. Supporting information

Supplementary data associated with this article can be found in the online version at [doi:10.1016/j.apcatb.2024.124090](https://doi.org/10.1016/j.apcatb.2024.124090).

## References

- X.P. Tao, Y. Zhao, S.Y. Wang, C. Li, R.G. Li, Recent advances and perspectives for solar-driven water splitting using particulate photocatalysts, *Chem. Soc. Rev.* 51 (2022) 3561–3608.
- Z. Wang, C. Li, K. Domen, Recent developments in heterogeneous photocatalysts for solar-driven overall water splitting, *Chem. Soc. Rev.* 48 (2019) 2109–2125.
- B. Samanta, A. Morales-García, F. Illas, N. Goga, J.A. Anta, S. Calero, A. Bieberle-Hütter, F. Libisch, A.B. Muñoz-García, M. Pavone, M.C. Toroker, Challenges of modeling nanostructured materials for photocatalytic water splitting, *Chem. Soc. Rev.* 51 (2022) 3794–3818.
- P. Zhou, I.A. Navid, Y.J. Ma, Y.X. Xiao, P. Wang, Z.W. Ye, B.W. Zhou, K. Sun, Z. T. Mi, Solar-to-hydrogen efficiency of more than 9% in photocatalytic water splitting, *Nature* 613 (2023) 66–70.
- D. Liu, J. Yao, S.T. Chen, J. Zhang, R.J. Li, T.Y. Peng, Construction of rGO-coupled  $\text{C}_3\text{N}_4/\text{C}_3\text{N}_5$  2D/2D Z-scheme heterojunction to accelerate charge separation for efficient visible light  $\text{H}_2$  evolution, *Appl. Catal. B Environ.* 318 (2022) 121822.
- X. Han, L. An, Y. Hu, Y.G. Li, C.Y. Hou, H.Z. Wang, Q.H. Zhang,  $\text{Ti}_{3-\text{x}}\text{MXene}$ -derived carbon-doped  $\text{TiO}_2$  coupled with  $\text{g-C}_3\text{N}_4$  as the visible-light photocatalysts for photocatalytic  $\text{H}_2$  generation, *Appl. Catal. B Environ.* 265 (2020) 118539.
- Q.Y. Li, F.J. Zhao, C. Qu, Q.Y. Shang, Z.H. Xu, L. Yu, J.R. McBride, T.Q. Lian, Two-dimensional morphology enhances light-driven  $\text{H}_2$  generation efficiency in  $\text{CdS}$  nanoplatelet-Pt heterostructures, *J. Am. Chem. Soc.* 140 (2018) 11726–11734.
- X.H. Zhang, T.Y. Peng, S.S. Song, Recent advances in dye-sensitized semiconductor systems for photocatalytic hydrogen production, *J. Mater. Chem. A* 4 (2016) 2365–2402.
- J.M. Wang, L.L. Guo, L. Xu, P. Zeng, R.J. Li, T.Y. Peng, Z-scheme photocatalyst based on porphyrin derivative decorated few-layer  $\text{BiVO}_4$  nanosheets for efficient visible-light-driven overall water splitting, *Nano Res.* 14 (2021) 1294–1304.
- H.S. Moon, K.C. Hsiao, M.C. Wu, Y.J. Yun, Y.J. Hsu, K.J. Yong, Spatial separation of cocatalysts on Z-scheme organic/inorganic heterostructure hollow spheres for enhanced photocatalytic  $\text{H}_2$  evolution and in-depth analysis of the charge-transfer mechanism, *Adv. Mater.* 35 (2023) 2200172.
- L.F. Liu, S.W. Du, X.Y. Guo, Y.J. Xiao, Z.X. Yin, N.C. Yang, Y.F. Bao, X.J. Zhu, S. Y. Jin, Z.C. Feng, F.X. Zhang, Water-stable nickel metal-organic framework nanobelts for cocatalyst-free photocatalytic water splitting to produce hydrogen, *J. Am. Chem. Soc.* 144 (2022) 2747–2754.
- C.Y. Wang, Y. Tang, Z.K. Geng, Y.C. Guo, X. Tan, Z.F. Hu, T. Yu, Modulating charge accumulation via electron interaction for photocatalytic hydrogen evolution: a case of fabricating palladium sites on  $\text{ZnIn}_2\text{S}_4$  nanosheets, *ACS Catal.* 13 (2023) 11687–11696.
- S.Q. Zhang, Z.F. Zhang, Y.M. Si, B. Li, F. Deng, L.X. Yang, X. Liu, W.L. Dai, S.L. Luo, Gradient hydrogen migration modulated with self-adapting S vacancy in copper-doped  $\text{ZnIn}_2\text{S}_4$  nanosheet for photocatalytic hydrogen evolution, *ACS Nano* 15 (2021) 15238–15248.
- X.C. Jiao, Z.W. Chen, X.D. Li, Y.F. Sun, S. Gao, W.S. Yan, C.M. Wang, Q. Zhang, Y. Lin, Y. Luo, Y. Xie, Defect-mediated electron–hole separation in one-unit-cell  $\text{ZnIn}_2\text{S}_4$  layers for boosted solar-driven  $\text{CO}_2$  reduction, *J. Am. Chem. Soc.* 139 (2017) 7586–7594.
- Q.J. Luan, X.D. Xue, R.J. Li, L. Gu, W.J. Dong, D.X. Zhou, X. Wang, B.Z. Li, G. Wang, C.M. Hou, Boosting photocatalytic hydrogen evolution: orbital redistribution of ultrathin  $\text{ZnIn}_2\text{S}_4$  nanosheets via atomic defects, *Appl. Catal. B Environ.* 305 (2022) 121007.
- Y.X. Li, P. Han, Y.L. Hou, S.Q. Peng, X.J. Kuang, Oriented  $\text{Zn}_m\text{In}_2\text{S}_{m+3}/\text{In}_2\text{S}_3$  heterojunction with hierarchical structure for efficient photocatalytic hydrogen evolution, *Appl. Catal. B Environ.* 244 (2019) 604–611.
- J.M. Wang, L. Xu, T.X. Wang, R.J. Li, Y.X. Zhang, J. Zhang, T.Y. Peng, Porphyrin conjugated polymer grafted onto  $\text{BiVO}_4$  nanosheets for efficient Z-scheme overall water splitting via cascade charge transfer and single-atom catalytic sites, *Adv. Energy Mater.* 11 (2021) 2003575.
- G.T. Sun, Z.G. Tai, F. Li, Q. Ye, T. Wang, Z.Y. Fang, L.C. Jia, W. Liu, H.Q. Wang, Construction of  $\text{ZnIn}_2\text{S}_4/\text{CdS}/\text{PdS}$  S-scheme heterostructure for efficient photocatalytic  $\text{H}_2$  production, *Small* 19 (2023) 2207758.
- D.L. Huang, S. Chen, G.M. Zeng, X.M. Gong, C.Y. Zhou, M. Cheng, W.J. Xue, X. L. Yan, J. Li, Artificial Z-scheme photocatalytic system: what have been done and where to go? *Coord. Chem. Rev.* 385 (2019) 44–80.
- Q.L. Xu, L.Y. Zhang, B. Cheng, J.J. Fan, J.G. Yu, S-scheme heterojunction photocatalyst, *Chem* 6 (2020) 1543–1559.
- E. Nikoloudakis, I. López-Duarte, G. Charalambidis, K. Ladomenou, M. Ince, A. G. Coutsopoulos, Porphyrins and phthalocyanines as biomimetic tools for photocatalytic  $\text{H}_2$  production and  $\text{CO}_2$  reduction, *Chem. Soc. Rev.* 51 (2022) 6965–7045.
- P. Zeng, L. Xu, H.Y. Jia, C.E. Liang, R.J. Li, T.Y. Peng, Porphyrin conjugated polymer/Pt-loaded graphite carbon nitride nanocomposites for efficient charge separation and broadband responsive  $\text{H}_2$  evolution, *Nanotechnology* 34 (2023) 315402.
- Y. Zheng, J.M. Wang, J. Zhang, T.Y. Peng, R.J. Li, Syntheses of asymmetric zinc porphyrins bearing different pseudo-pyridine substituents and their photosensitization for visible-light-driven  $\text{H}_2$  production activity, *Dalton Trans.* 46 (2017) 8219–8228.
- J.M. Wang, D. Liu, Q.W. Liu, T.Y. Peng, R.J. Li, S.Y. Zhou, Effects of the central metal ions on the photosensitization of metalloporphyrins over carbon nitride for visible-light-responsive  $\text{H}_2$  production, *Appl. Surf. Sci.* 464 (2019) 255–261.
- G.C. Zuo, Y.T. Wang, W.L. Teo, A.M. Xie, Y. Guo, Y.X. Dai, W.Q. Zhou, D. Jana, Q. M. Xian, W. Dong, Y.L. Zhao, Ultrathin  $\text{ZnIn}_2\text{S}_4$  nanosheets anchored on  $\text{Ti}_3\text{C}_2\text{T}_x$  MXene for photocatalytic  $\text{H}_2$  evolution, *Angew. Chem. Int. Ed.* 59 (2020) 11287–11292.
- X.W. Shi, C. Dai, X. Wang, J.Y. Hu, J.Y. Zhang, L.X. Zheng, L. Mao, H.J. Zheng, M. S. Zhu, Protruding Pt single-sites on hexagonal  $\text{ZnIn}_2\text{S}_4$  to accelerate photocatalytic hydrogen evolution, *Nat. Commun.* 13 (2022) 1287.
- B. Chai, T.Y. Peng, P. Zeng, X.H. Zhang, Preparation of a MWCNTs/  $\text{ZnIn}_2\text{S}_4$  composite and its enhanced photocatalytic hydrogen production under visible-light irradiation, *Dalton Trans.* 41 (2012) 1179–1186.
- S.B. Wang, B.Y. Guan, X. Wang, X.W.D. Lou, Formation of hierarchical  $\text{Co}_9\text{S}_8@ \text{ZnIn}_2\text{S}_4$  heterostructured cages as an efficient photocatalyst for hydrogen evolution, *J. Am. Chem. Soc.* 140 (2018) 15145–15148.
- T.M. Su, C.Z. Men, L.Y. Chen, B.X. Chu, X. Luo, H.B. Ji, J.H. Chen, Z.Z. Qin, Sulfur vacancy and  $\text{Ti}_3\text{C}_2\text{T}_x$  cocatalyst synergistically boosting interfacial charge transfer in 2D/2D  $\text{Ti}_3\text{C}_2\text{T}_x/\text{ZnIn}_2\text{S}_4$  heterostructure for enhanced photocatalytic hydrogen evolution, *Adv. Sci.* 9 (2022) 2103715.
- C. Du, B. Yan, G.W. Yang, Self-integrated effects of 2D  $\text{ZnIn}_2\text{S}_4$  and amorphous  $\text{Mo}_2\text{C}$  nanoparticles composite for promoting solar hydrogen generation, *Nano Energy* 76 (2020) 105031.
- Y.Y. Zhang, S.T. Chen, Y.X. Zhang, R.J. Li, B. Zhao, T.Y. Peng, Hydrogen-bond regulation of the microenvironment of Ni(II)-porphyrin bifunctional electrocatalysts for efficient overall water splitting, *Adv. Mater.* 35 (2023) 2210727.
- H. Dotan, K. Sivula, M. Grätzel, A. Rothschild, S.C. Warren, Probing the photoelectrochemical properties of hematite ( $\alpha\text{-Fe}_2\text{O}_3$ ) electrodes using hydrogen peroxide as a hole scavenger, *Energy Environ. Sci.* 4 (2011) 958–964.
- D.K. Zhong, S.J. Choi, D.R. Gamelin, Near-complete suppression of surface recombination in solar photoelectrolysis by “Co-PI” catalyst-modified  $\text{W:BiVO}_4$ , *J. Am. Chem. Soc.* 133 (2011) 18370–18377.
- W.W. Xu, W.C. Gao, L.X. Meng, W. Tian, L. Li, Incorporation of sulfate anions and sulfur vacancies in  $\text{ZnIn}_2\text{S}_4$  photoanode for enhanced photoelectrochemical water splitting, *Adv. Energy Mater.* 11 (2021) 2101181.
- Y. Nosaka, A.Y. Nosaka, Generation and detection of reactive oxygen species in photocatalysis, *Chem. Rev.* 117 (2017) 11302–11336.
- M. Dongol, A. E-Denglawey, A.F. Elhady, A.A. Abuelwafa, Structural properties of nano 5, 10, 15, 20-tetraphenyl-21H,23H-porphine nickel (II) thin films, *Curr. Appl. Phys.* 12 (2012) 1334–1339.
- S.H. Shen, L. Zhao, X.J. Guan, L.J. Guo, Improving visible-light photocatalytic activity for hydrogen evolution over  $\text{ZnIn}_2\text{S}_4$ : a case study of alkaline-earth metal doping, *J. Phys. Chem. Solids* 73 (2012) 79–83.
- A.M. El-Mahalawy, A.M. Nawar, A.R. Wassel, Efficacy assessment of metalloporphyrins as functional materials for photodetection applications: role of central tetrapyrrole metal ions, *J. Mater. Sci.* 57 (2022) 15413–15439.
- Y. Sun, J. Wu, Z. Zhang, Q.L. Liao, S.C. Zhang, X. Wang, Y. Xie, K.K. Ma, Z. Kang, Y. Zhang, Phase reconfiguration of multivalent nickel sulfides in hydrogen evolution, *Energy Environ. Sci.* 15 (2022) 633–644.
- O.O. Balayeva, A.A. Azizov, M.B. Muradov, A.M. Maharramov, G.M. Eyyazova, R. M. Alosmanov, Z.Q. Mamiyev, Z.A. Aghamaliyev,  $\beta\text{-NiS}$  and  $\text{Ni}_3\text{S}_4$  nanostructures: fabrication and characterization, *Mater. Res. Bull.* 75 (2016) 155–161.
- D.M. Eby, K. Artyushkova, A.K. Paravastu, G.R. Johnson, Probing the molecular structure of antimicrobial peptide-mediated silica condensation using X-ray photoelectron spectroscopy, *J. Mater. Chem.* 22 (2012) 9875–9883.
- A. Wolberg, J. Manassen, Electron paramagnetic resonance identification of a nickel(III) compound produced by electrochemical oxidation of nickel(II) tetraphenylporphyrin, *Inorg. Chem.* 9 (1970) 2365–2367.

[43] X. Wang, X.L. Zhang, W. Zhou, L.Q. Liu, J.H. Ye, D.F. Wang, An ultrathin porphyrin-based metal-organic framework for efficient photocatalytic hydrogen evolution under visible light, *Nano Energy* 62 (2019) 250–258.

[44] R. Golnak, J. Xiao, M. Pohl, C. Schwanke, A. Neubauer, K.M. Lange, K. Atak, E. F. Aziz, Influence of the outer ligands on metal-to-ligand charge transfer in solvated manganese porphyrins, *Inorg. Chem.* 55 (2016) 22–28.

[45] Y.X. Li, M.F. Ji, Z.Y. Ma, L.H. Meng, R.C. He, S.Q. Peng, Hierarchically porous polymeric carbon nitride as a volume photocatalyst for efficient H<sub>2</sub> generation under strong irradiation, *Sol. RRL* 6 (2022) 2100823.

[46] S.H. Shen, J. Chen, X.X. Wang, L. Zhao, L.J. Guo, Microwave-assisted hydrothermal synthesis of transition-metal doped ZnIn<sub>2</sub>S<sub>4</sub> and its photocatalytic activity for hydrogen evolution under visible light, *J. Power Sources* 196 (2011) 10112–10119.

[47] P. Zeng, H.R. Liu, H.Y. Jia, J.Y. Cai, X.E. Deng, T.Y. Peng, In-situ synthesis of single-atom CoN<sub>x</sub> clusters-decorated TiO<sub>2</sub> for highly efficient charge separation and CO<sub>2</sub> photoreduction, *Appl. Catal. B Environ.* 340 (2024) 123268.

[48] D. Tafalla, P. Salvador, R.M. Benito, Kinetic approach to the photocurrent transients in water photoelectrolysis at n-TiO<sub>2</sub> electrodes: II. Analysis of the photocurrent-time dependence, *J. Electrochem. Soc.* 137 (1990) 1810–1815.

[49] J.T. Li, S.K. Cushing, P. Zheng, F.K. Meng, D. Chu, N.Q. Wu, Plasmon-induced photonic and energy-transfer enhancement of solar water splitting by a hematite nanorod array, *Nat. Commun.* 4 (2013) 2651.